

Characterization of materials and film stacks for accurate surface topography measurement using a white-light optical profiler

X. Colonna de Lega* and Peter J. de Groot
Zygo Corporation, 21 Laurel Brook Rd, Middlefield, CT, USA 06455

ABSTRACT

Pupil-Plane Scanning White-Light Interferometry measures reflectivity as a function of angle of incidence, wavelength and polarization in one location of an object surface. This information is converted into ellipsometric information and allows the characterization of material optical properties and layer thickness in the case of layered structures. We illustrate the capability of the method by measuring the thickness and refractive index of thin film standards. The information is also used to create accurate 3D topography maps of complex object structures.

Keywords: interference microscopy, topography, white-light, material characterization, thin films

INTRODUCTION

Scanning White-Light Interference (SWLI) microscopy¹ is a mature technology used by a wide range of industries for non-contact, high-speed 3D surface metrology. The typical interference microscope offers a large choice of magnifications (from 0.5X to 100X) and provides sub-nm resolution topography measurements with high-reproducibility over a variety of surface types, including patterned semiconductor wafers, flat panel display components,^{2,3} automotive machined metal parts,⁴ transparent film structures, MEMS devices, etc.

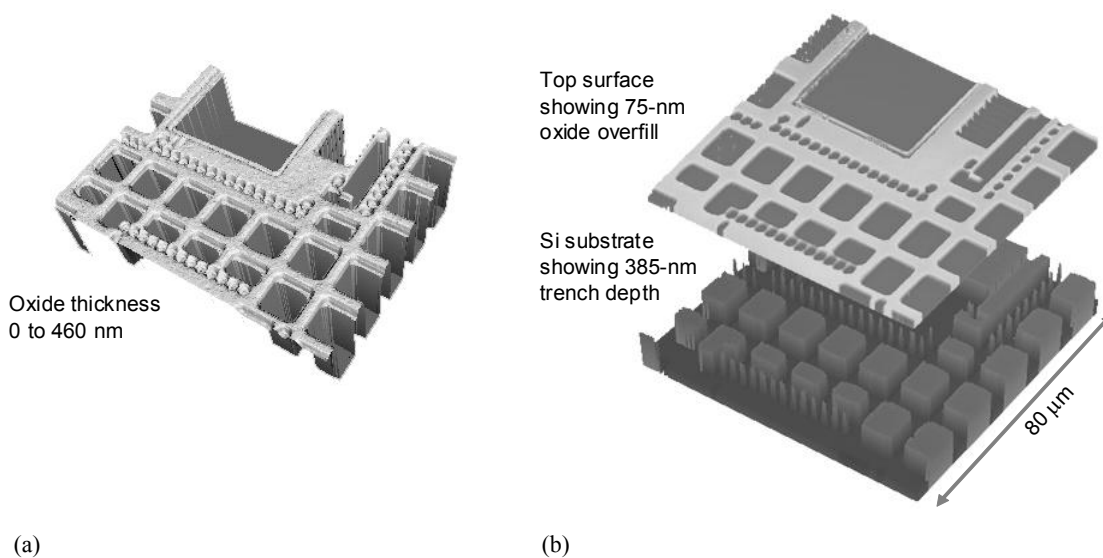


Figure 1. (a) 3D film thickness profile generated with model-based SWLI for an oxide film on patterned silicon substrate. (b) Corresponding topography map for the top surface and buried interface of the film. In this paper, we consider an alternative white-light interferometer geometry that collects information about a single point in the film resolved independently for wavelength, angle of incidence, and polarization.

* xcolonna@zygo.com

For many of these applications topography measurements are performed over multiple object areas covered with dissimilar materials or film stacks. The phase change on reflection (PCOR) of the reflected light and its variations as a function of wavelength and angle of incidence for high-NA objectives directly affect the reported topography by introducing material and film-dependent height offsets. In prior work, we have shown that detailed interference signal modeling (1) identifies materials and films and (2) provide accurate topography by matching model and experimental signals^{5,6,7}. We call this approach "modeled-based SWLI." Figure 1 shows a 3D map of film thickness as well as topography maps of the air / film and film / substrate interfaces in the case of a transparent oxide film on silicon.⁸

In this paper we present a complementary approach that aims at leveraging differently the information contained in the SWLI interference signals. This technique trades the ability described above to resolve information at multiple object locations with the ability to measure the surface reflectivity in one location as a function of angle of incidence, polarization state and wavelength. The corresponding wealth of information enhances the ability to characterize materials and film stacks. A key point is that this additional functionality requires no significant modification of the interference microscope and that the topography measurement capability described earlier is preserved. Better yet, the new functionality can be combined with other measurement modes, for instance by providing information about the optical properties or nominal thickness of films present on the object surface.

PUPIL-PLANE SCANNING WHITE-LIGHT INTERFEROMETRY

A known approach to rapidly collecting data over a wide range of angles is to image the pupil (or back focal plane) of a high-NA microscope objective onto a camera.⁹ High-NA, pupil-plane imaging provides the angle-resolved optical properties of surfaces at a single, focused measurement point.^{10,11,12,13} Here we add the extra dimension of wavelength by mathematical decomposition of a white-light interference pattern collected at the pupil plane.¹⁴

We call our technique PUPil-Plane SWLI or PUPS. Figure 2 shows how the tube lens that would normally image the object surface onto the detector has been replaced by a relay lens that images the exit pupil of the Mirau microscope objective onto the detector. The field stop defines a 10- to 20- μm diameter point of interest on the object surface. A linear polarizer close to the microscope objective acts both as a polarizer for the illumination light and an analyzer for the reflected light.

The detector is a CCD or CMOS camera. Just as in the more familiar SWLI geometry for surface topography, a series of frames is collected during a linear scan of the microscope objective along its optical axis. The light source is for example a white-light LED or an arc lamp providing a wide range of wavelengths within the sensitivity band of the detector. The scan length is typically selected to exceed the coherence length of the light source.

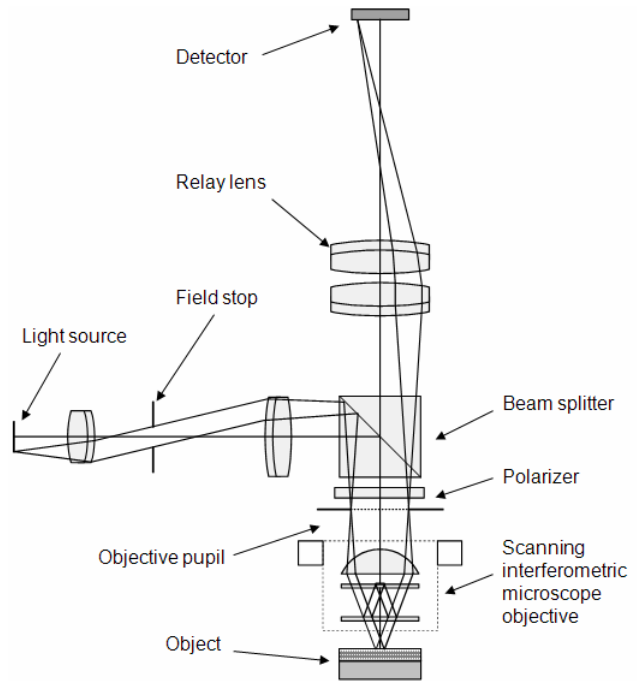


Figure 2. White-light interference microscope (Mirau-type) configured for pupil imaging.

INFORMATION CONTENT OF THE PUPIL INTERFEROGRAM

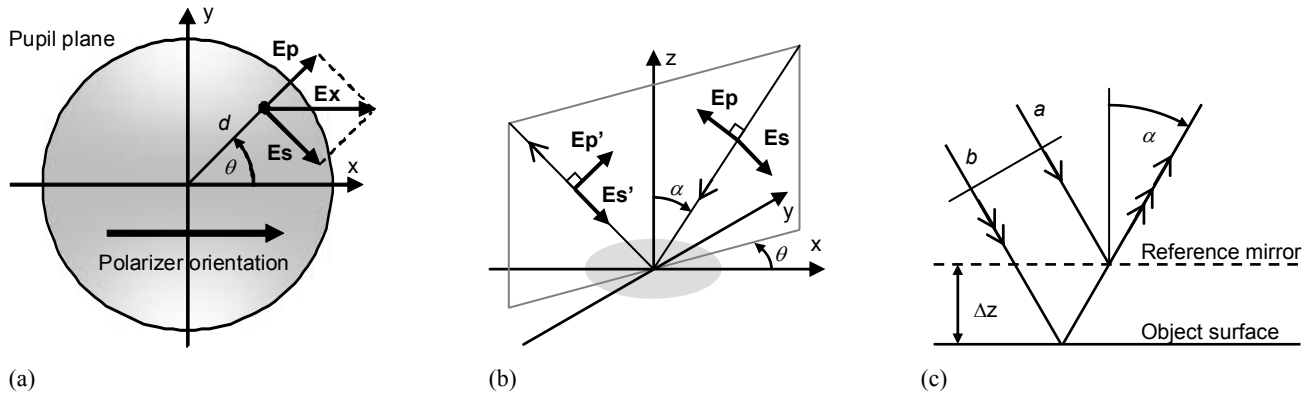


Figure 3. (a) Coordinate system at the pupil. (b) Coordinate system at the object. (c) Object and reference rays.

Figure 3(a) defines a coordinate system at the pupil of the microscope objective. The light source is nominally imaged onto this plane by the illumination optics. A source point defined by a radial distance d and azimuth angle θ defines the plane of incidence for the light that will propagate from this source point, transmit through the objective and reflect of the object surface (Figure 3(b)). The polarizer is aligned parallel to the X-axis in this example. The polarization state is common at all locations at the pupil and is represented by a vector \mathbf{E}_x . Its projections \mathbf{E}_p and \mathbf{E}_s onto the plane of incidence and perpendicular to that same plane define the usual P and S polarization states for the illumination beam. A source point located on the X-axis emits light that is confined to the P polarization state. Similarly, a source point located on the Y-axis emits light confined to the S polarization state. Other azimuthal locations correspond to a varying mix of S and P, yielding a varying elliptical polarization state for the illumination. The salient point is that the system effectively “probes” the complex reflectivity of the object surface by illuminating it with varying polarization states.

The radial distance d of a source point at the pupil defines the angle of incidence α of the wavefront generated by the source point in object space. In the case of a well-corrected optical system the Abbé sine condition provides a simple relationship between the two quantities: $d = F \sin \alpha$, where F is the focal length of the microscope objective.

Figure 3(c) illustrates the paths of two rays a and b coming from a given source point at the pupil. Ray a bounces off from the reference mirror of the interferometer with an angle of incidence α . The ray is shown in the figure as bouncing from the virtual image of the reference mirror. Ray b comes from the same source point and thus travels parallel to a in object space. When the object surface is moved by a distance Δz from the virtual image of the reference mirror, ray b has to travel an extra optical path length $2\Delta z \cos \alpha$, and the corresponding phase shift for the interferogram generated at a source wavelength λ is: $\Delta \phi = 2k\Delta z \cos \alpha$, where $k = 2\pi/\lambda$.

During data acquisition the objective is scanned linearly along its optical axis and interference signals are captured by the detector at every pupil location. The formula above implies that the interferometric signal recorded for a monochromatic light source has an angular frequency $2k \cos \alpha$ with respect to the scan variable z . If the source spectrum is broad the interferometric signal at a given pupil position can be described as the superposition of the multiple interferograms generated by the multiple spectral components of the source.⁵ In practice, a Fourier transformation of the interference signal with respect to z yields a range of angular frequencies that can be mapped back to actual source spectral components when the angle of incidence α is known. This is another key advantage of PUPS: all the wavelengths present in the source spectrum are measured simultaneously. They are separated during data processing by Fourier transformation of the interference signal. Hence, no extra optical components (such as dispersive prisms, gratings, etc) are required to separate the spectral components and the two-dimensional detector can be fully dedicated to resolving angle of incidence and azimuth information.

In summary, we have the quite remarkable result that PUPS collects multi-spectral data over a range of polarization states and angles of incidence in a *single* measurement. The angular information is spatially separated in the image of the

pupil and the spectral information is separated by Fourier transformation of the interference signal. This wealth of information can be used advantageously to derive optical properties of unknown materials or film stacks, as shown in the next sections.

FROM INTERFEROMETRY TO ELLIPSOMETRY

Pupil points that are located on the axis defined by the polarizer or on a perpendicular axis correspond to locations where the polarization of the illumination light at the object is linear and either within or perpendicular to the plane of incidence. It follows that the interference signal magnitude measured during the scan is directly proportional to the magnitude of the object reflection coefficient for P or S polarization, r_p and r_s respectively. The difference of the phase values measured for interferograms captured with S and P polarizations is the difference of the phases of the reflection coefficients themselves. Based on these observations we define a simple procedure that yields the ratio of the P and S complex reflection coefficients:

- Pick two pixels in the image of the pupil that are at the same distance from the optical axis, one located on the X-axis, the other located on the Y-axis. The radial distance from the optical axis defines the angle of incidence α .
- Fourier transform the interference signals measured at these two locations and extract the spectral components corresponding to a chosen source wavelength λ (the corresponding signal frequency is $2k\cos\alpha$).
- Calculate the ellipsometry ratio $\rho = r_p / r_s$ of the two spectral components for the chosen angle of incidence and wavelength.

Depending on the application the simple procedure outlined here is repeated for other wavelengths and angles of incidence. Any of the widely-known procedures, algorithms or software methods developed to derive optical properties from ellipsometric measurements can be applied directly to the data that we extract from the pupil interferogram. The step of deriving ellipsometric ratios results in a significant data reduction. The outcome is a cloud of measured ratios as a function of angle of incidence and wavelength. This is the basis of material and film analyses similar to those performed with Variable Angle Spectral Ellipsometry.¹⁵ In this context, it is useful to model and analyze the sensitivity of the ellipsometric ratio to the parameters of interest such as refractive index or thickness. The goal is to identify the combination of angles of incidence and wavelengths that maximize the performance of the system for these parameters. The benefit of PUPS is that it provides in a single measurement a wide range of angles and wavelengths to choose from.

In practice, a system characterization using a set of known reference samples enhances accuracy. The information gathered in this step can account for instance for variations of the light source intensity distribution across the pupil. Further, we take advantage of clear symmetries in the pupil-plane data distribution to reduce uncorrelated noise terms.

FROM ELLIPSOMETRIC RATIO TO OPTICAL PROPERTIES

This section provides a rapid overview of how the ellipsometric ratio information relates to the optical properties of bulk materials and film stacks as well as film thickness in the latter case.¹⁶

The ellipsometric ratio is usually expressed as two angles, Δ and Ψ :

$$\rho(\alpha, k) = \frac{r_p(\alpha, k)}{r_s(\alpha, k)} = \tan(\Psi(\alpha, k)) \exp(i\Delta(\alpha, k)) \quad (1)$$

In the case of the characterization of a bulk sample the material complex refractive index can be obtained readily using:

$$n(k) = n_0 \tan(\alpha) \sqrt{1 - \frac{4\rho(\alpha, k)}{(1 + \rho(\alpha, k))^2} \sin(\alpha)^2} \quad (2)$$

where n_0 is the refractive index of the ambient medium (usually air).

In the case of a transparent monolayer with known refractive indices n_0 , n_1 , n_2 for the ambient, film and substrate materials the following equations yield the unknown film thickness t :

$$\begin{aligned}
\alpha_0 &= \alpha, & \alpha_1 &= \frac{n_0(k)}{n_1(k)} \sin(\alpha_0), & \alpha_2 &= \frac{n_1(k)}{n_2(k)} \sin(\alpha_1) \\
r_{01p} &= \frac{\tan(\alpha_0 - \alpha_1)}{\tan(\alpha_0 + \alpha_1)}, & r_{12p} &= \frac{\tan(\alpha_1 - \alpha_2)}{\tan(\alpha_1 + \alpha_2)} \\
r_{01s} &= -\frac{\sin(\alpha_0 - \alpha_1)}{\sin(\alpha_0 + \alpha_1)}, & r_{12s} &= -\frac{\sin(\alpha_1 - \alpha_2)}{\sin(\alpha_1 + \alpha_2)} \\
A &= r_{01p}, & B &= r_{12p} + r_{01p}r_{01s}r_{12s}, & C &= r_{12p}r_{01s}r_{12s} \\
D &= r_{01s}, & E &= r_{12s} + r_{01p}r_{01s}r_{12p}, & F &= r_{01p}r_{12p}r_{12s} \\
X &= \frac{-(B - \rho(\alpha, k)E) \pm \sqrt{(B - \rho(\alpha, k)E)^2 - 4(C - \rho(\alpha, k)F)(A - \rho(\alpha, k)D)}}{2(C - \rho(\alpha, k)F)} \\
t &= \frac{i \log(X)}{2kn_1(\lambda)\cos(\alpha_1)}
\end{aligned} \tag{3}$$

The material properties required for this calculation are derived from measurements of representative bulk samples or using tabulated data found in the literature.¹⁷

For more complex cases (e.g. larger number of unknown parameters) analytical solutions are no longer available and numerical optimization techniques are used to determine unknown optical properties and film thicknesses. A common option is to define a chi-square target function such as:

$$\chi^2(P) = \sum_i (\Psi_i - \Psi_m(\alpha_i, k_i, P))^2 + \sum_i (\Delta_i - \Delta_m(\alpha_i, k_i, P))^2 \tag{4}$$

where the vector P contains estimates of the unknown parameters being sought and the summation over i corresponds to the use of multiple combinations of angles of incidence and source wavelengths (α_i, k_i) . The functions Ψ_m and Δ_m are model functions used to compute ellipsometric parameters to be compared to the measured values Ψ_i and Δ_i . In the case of a multilayer film stack the scattering matrix technique (see chapter 4 in Ref.[16]) is used to calculate the modeled reflection coefficients rs_m and rp_m from which Ψ_m and Δ_m are calculated. Depending on the application P might contain multiple film thickness estimates, refractive index values for all the wavenumbers of interest and/or model parameters used in analytical refractive index models.¹⁸

Various algorithms can be applied in practice to minimize the function defined in Eq.(4), for example a simplex or Levenberg-Marquardt solver.¹⁹ We use both home-grown processing programs developed in Mathcad and commercial ellipsometry software²⁰ to process the experimental data presented in the next sections.

EXPERIMENTAL RESULTS: FILM THICKNESS MEASUREMENTS

We first report experimental results for the measurement of certified film thickness standards. These standards are single layer films of silicon dioxide or silicon nitride on silicon substrates. The first two lines of Table 1 show the certified thickness values and 2- σ uncertainties for single-wavelength ellipsometric measurements assuming fixed material properties. The following lines show the measured thickness using PUPS. The white-light interference microscope used here provides a 20°-50° angular range and 450-650 nm wavelength range. The repeatability and bias of the measured values are derived from a series of 32 successive measurements. For these measurements the optical properties of the films and substrate are assumed known and fixed to published values.^{21,17}

Table 1. Film thickness standard certified values and uncertainties provided by the manufacturer compared to measured values using the white-light interference microscope (optical properties are assumed known). The statistics are derived from 32 successive measurements.

	SiO2 on Si samples								Si3N4 on Si samples				
Certified thickness (nm)	8.7	12.3	44.1	96.6	182.8	396.1	675.2	1003.4	18.7	50.6	91.5	123.0	201.5
Thick. Uncertainty (nm)	0.4	1.2	1.0	0.4	0.5	2.0	0.9	0.9	0.3	0.4	0.4	1.4	1.7
PUPS thickness (nm)	8.9	12.8	43.9	97.2	182.7	395.3	674.2	1002.4	19.3	46.7	90.1	122.6	198.0
Standard deviation (nm)	0.05	0.04	0.08	0.09	0.10	0.19	0.40	0.30	0.04	0.04	0.06	0.08	0.11
% Standard deviation	0.59	0.34	0.18	0.09	0.05	0.05	0.06	0.03	0.19	0.08	0.07	0.07	0.06
Bias (nm)	0.21	0.48	-0.17	0.64	-0.14	-0.81	-1.00	-1.02	0.58	-3.93	-1.44	-0.40	-3.54
% Bias	2.4	3.8	-0.4	0.7	-0.1	-0.2	-0.1	-0.1	3.0	-8.4	-1.6	-0.3	-1.8

These results show a typical 0.1% thickness repeatability for oxide films that are 100-nm thick or more and nitride films that are 50-nm thick or more. The typical measurement bias is less than 1% for oxide and 2% for nitride films 100-nm thick or more. The larger bias for the nitride films is mostly due to the assumed optical properties that don't quite match those used by the film standard manufacturer.

Figure 4 shows graphically the results of Table 1 for the oxide films. The plot shows the bias of the interferometric measurement as well as the $\pm 2\sigma$ repeatability of the measurement as error bars. This can be loosely compared to the $\pm 2\sigma$ uncertainty values provided by the standards manufacturer. Note that a proper uncertainty budget for the interferometric measurement should include both the estimated bias and repeatability reported here.

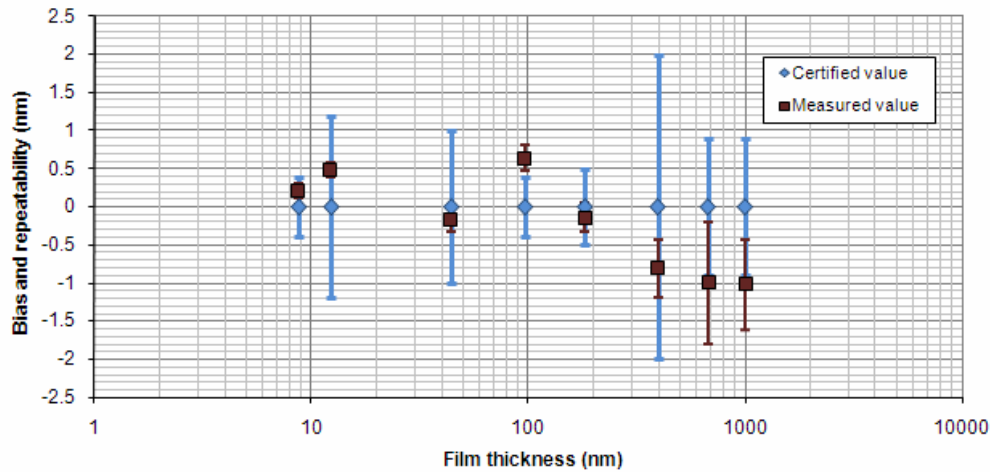


Figure 4. Plot showing the difference between the certified value and average measured value of the thickness of the oxide standards (square markers). The associated error bars correspond to the $\pm 2\sigma$ standard deviation of the measurement. The $\pm 2\sigma$ uncertainty of the certified values (manufacturer data) are represented as error bars centered on the zero-bias line (diamond markers).

Table 2 shows the results of processing the same data without assuming that the film optical properties are known. In this case a three-parameter Cauchy model is used to describe the material dispersion. These three parameters are optimized simultaneously with film thickness. Because of this larger number of degrees of freedom the repeatability of the measured thickness becomes larger by about a factor of three. Nevertheless, the technique still provides reasonably accurate estimates of the film thickness for most of the films tested here.

Table 2. Film thickness standard certified values and uncertainties provided by the manufacturer compared to measured values using the white-light interference microscope. A floating three-parameter Cauchy model describing the film optical properties is optimized simultaneously with the film thickness for these data.

	SiO2 on Si samples								Si3N4 on Si samples				
Certified thickness (nm)	8.7	12.3	44.1	96.6	182.8	396.1	675.2	1003.4	18.7	50.6	91.5	123.0	201.5
Thick. Uncertainty (nm)	0.4	1.2	1.0	0.4	0.5	2.0	0.9	0.9	0.3	0.4	0.4	1.4	1.7
PUPS thickness (nm)	7.3	10.5	41.9	97.3	179.5	395.7	676.2	1013.3	19.3	50.4	90.2	119.5	199.4
Standard deviation (nm)	0.11	0.06	0.35	0.07	0.85	0.61	0.94	0.67	0.03	0.10	0.14	0.84	0.19
% Standard deviation	1.49	0.56	0.84	0.08	0.47	0.15	0.14	0.07	0.16	0.19	0.15	0.70	0.09
Bias (nm)	-1.35	-1.85	-2.18	0.74	-3.27	-0.41	1.02	9.90	0.58	-0.18	-1.32	-3.53	-2.09
% Bias	-18.4	-17.7	-5.2	0.8	-1.8	-0.1	0.2	1.0	3.0	-0.4	-1.5	-3.0	-1.0

In another experiment we characterize the thickness of a three-layer film stack made of SiO₂ on Cu on SiO₂ on Si. We use a three-parameter Cauchy model to describe the optical properties of the dioxide layers and tabulated data for copper. The data regression optimizes three material parameters and three unknown thicknesses. The same sample was sent to a laboratory for ellipsometric characterization using a variable angle spectroscopic ellipsometer. The measured thickness for each layer is reported in Table 3, illustrating the reasonable agreement between the two instruments.

Table 3. Comparison of multi-layer film thickness measurement using PUPS and an ellipsometer

Layer	Interferometer	VASE
SiO2	207 nm	211 nm
Cu	18.4 nm	17.6 nm
SiO2	354 nm	360 nm

EXPERIMENTAL RESULTS: STEP HEIGHT MEASUREMENT

The previous section illustrates the capability of PUPS to determine the thickness and refractive index of one or more material layers. A possible application is to use this information to account for PCOR effects when performing surface topography measurements. In this section we measure the step between the bottom of an etched silicon trench and the top of the surrounding un-etched area, see Figure 5. The un-etched region is protected from etching by a 10-nm oxide layer covered by a nominally 85-nm thick nitride layer.

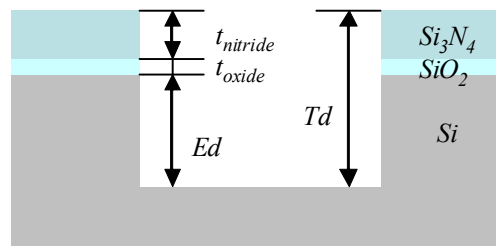


Figure 5. Trench etched in silicon. The un-etched areas are covered with a 10-nm thick thermal oxide layer covered by a nominally 85-nm thick nitride layer.

The goal of the experiment is to compare the total trench depth Td measured with an AFM to the total trench depth measured with the white-light interference microscope. The steps of this experiment are listed next.

- We first measure the physical step Td from the top of the nitride layer to the bottom of the trench using the AFM. The average reported step is 400.5 nm.
- We use the optical profiler in PUPS mode to collect (Δ, Ψ) data over the un-etched area. We derive from these data the thickness and parameters of a Cauchy model representing the unknown optical properties of the nitride layer. The oxide layer thickness is assumed known and equal to 10 nm. The reported thickness is $t_{\text{nitride}} = 83.5$ nm and the refractive index is 2.006 at a wavelength of 633 nm.
- We create a synthetic interference signal for the nitride on oxide on silicon film stack using the previously measured nitride refractive index and thickness. This is accomplished using the technique described in Ref.[5].
- The same procedure generates a synthetic interference signal for bare silicon, representing the bottom of the trench. Both signals are generated with the silicon interface at a common height within the synthetic scan data. In other words the two signals correspond to the sample configuration before etch.
- We apply a frequency-domain analysis (FDA) technique¹ to extract height information from the synthetic white-light signals. The nitride-covered region appears $\Delta h = 146.8$ nm higher than the bare silicon surface.
- Finally we measure the sample in imaging mode and use FDA to create a topography map of the trench. The measured trench depth reported by the optical profiler is $Td' = 456.5$ nm.

We can now compensate the topography map with the measured nitride thickness and its predicted PCOR-effect Δh to report an estimate of the physical trench depth. The table below compares the results obtained with the two instruments.

Table 4. Comparison of the trench depth measured with an AFM and the interference microscope.

	AFM	Microscope	
Trench depth	400.5 nm	456.5 nm	Measured step
		-146.8 nm	Height offset
		+93.5 nm	nitride + oxide thickness
Trench depth	400.5 nm	403.2 nm	Trench depth

We find that the two trench depths are within 3 nm of one another, representing a matching error smaller than 1%. The match can be improved by taking into account the fact that etched silicon grows a self-capping transparent oxide layer 1 or 2-nm thick over a period of days. This is too thin to affect the optical topography measurement and the height reported by the interference microscope corresponds to the oxide / silicon interface in the etched area. On the other hand, the AFM profiles the physical surface of the sample and reports the height of the air / oxide interface. Hence, we could correct the optical trench depth measurement by subtracting the optical thickness of the native oxide layer. This would bring the trench depth measured optically within about 1 nm of the depth reported by the AFM.

The agreement between AFM and optical profiler supports the assumption that the nitride film thickness is uniform over the topography measurement area. For applications where the thickness is expected to vary spatially a localized PUPS measurement provides the refractive index and modeled-based SWLI provides a map of the layer thickness.

In the case of a semiconductor etch process the critical dimension is usually the silicon etch depth Ed . An AFM or other mechanical profiler can only report the total trench depth Td . Some other metrology is thus required to measure the nitride and oxide film thicknesses and calculate etch depth. In contrast, a single white-light interference microscope combines topography and PUPS measurement modes that provide the equivalent functionality in one self-consistent platform.

SUMMARY AND PERSPECTIVES

We introduce here a pupil-plane SWLI method (PUPS) that provides angle-resolved, wavelength-resolved and polarization-resolved measurements of the reflectivity of a complex object surface. The only modification of the usual interference microscope configuration is the replacement of the tube lens by a relay lens and the addition of a polarizer to the interference microscope objective. The collected information converts to ellipsometry angles Δ and Ψ as a

function of wavelength and angle of incidence. This allows using the methodologies developed in the field of ellipsometry to derive the optical properties of materials over ranges of wavelengths, as well as the thickness of mono or multi-layer film stacks. The experimental data gathered on certified film standards illustrates nm-level measurement bias over the thickness range 10-1000 nm. Repeatability is better than 0.1% 1- σ for films thicker than 100 nm.

The information collected in PUPS mode can be readily used to enhance the accuracy of model-based SWLI topography techniques. An example shows nm-level agreement between SWLI and AFM measurements of a 400-nm deep trench in silicon in the presence of an unknown nitride film. The PUPS and SWLI topography measurement modes are easily combined into a single white-light interference microscope platform.

ACKNOWLEDGMENTS

The authors wish to acknowledge the contributions of the following individuals who developed the hardware platforms used for this research and were involved in critical experimental work: J. Beverage, J. Biegen, M. Fay, R. Kruse.

REFERENCES

- [1] de Groot, P. and Deck, L., "Surface profiling by analysis of white-light interferograms in the spatial frequency domain," *J. Mod. Opt.*, **42**(2), 389-401 (1995).
- [2] Grigg, D., Garden, R., Mino, M., Lu, L. and de Groot, P., "New optical metrology techniques for color filter inspection and process control," Proc. IDW 11th international display workshops, Niigata, Japan, (2004).
- [3] He, Z., Zheng, J., Garden, R. and de Groot, P., "New optical 3D-CD metrology techniques for liquid crystal display manufacture inspection and process control," Proc. Asia Display, Shanghai, China, (2007).
- [4] Wyant, J. C. , "How to extend interferometry for rough-surface tests," *Laser Focus World*, 131-135 (1993).
- [5] de Groot, P. and Colonna de Lega, X., "Signal modeling for low-coherence height-scanning interference microscopy," *Appl. Opt.* **43**(25), 4821-4830 (2004).
- [6] de Groot, P. and Colonna de Lega, X., "Signal modeling for modern interference microscopes," *Proc. SPIE 5457*, 26-34 (2004).
- [7] de Groot, P. and Colonna de Lega, X., "Angle-resolved three-dimensional analysis of surface films by coherence scanning interferometry," *Opt. Lett.* **32**(12), 1638-1640 (2007).
- [8] Colonna de Lega, X. and de Groot, P., "Optical Topography Measurement of Patterned Wafers," AIP ULSI Conference Proceedings 788, 432-436 (2005).
- [9] Pluta, M., *Advanced light microscopy*, Vol.3, Elsevier, Amsterdam, 265-271 (1993).
- [10] Shatalin, S. V., Juškaitis, R., Tan, J. B. and Wilson, T., "Reflection conoscopy and microellipsometry of isotropic thin film structures," *J. Microsc.* **179**, 241-252 (1995).
- [11] Rosencwaig, A., Opsal, J., Willenborg, D. L., Kelso, S. M. and Fanton, J. T., "Beam profile reflectometry: a new technique for dielectric film measurements," *Appl. Phys. Lett.* **60**, 1301-1303 (1992).
- [12] See, C. W., Somekh, M. G. and Holmes, R. D., "Scanning optical microellipsometer for pure surface profiling," *Appl. Opt.* **25**(34), 6663-6668 (1996).
- [13] Feke, G. D., Snow, D. P., Grober, R. D., de Groot, P. and Deck, L., "Interferometric back focal plane microellipsometry," *Appl. Opt.* **37**(10), 1796-1802 (1998).
- [14] Colonna de Lega, X. and de Groot, P., "Interferometer with multiple modes of operation for determining characteristics of an object surface," US Patent Application 20060158658 A1 (2006).
- [15] Woollam, J. A., Johs, B., Herzinger, C. M., Hilfiker, J., Synowicki, R. and Bungay, C. L., "Overview of Variable Angle Spectroscopic Ellipsometry (VASE), Part I: Basic Theory and Typical Applications," *Proc. SPIE CR72*, 3-28 (1999).
- [16] Azzam, R. M. A. and Bashara, N. M., *Ellipsometry and Polarized Light*, Elsevier Science B.V., (1987).
- [17] Palik, E. D., *Handbook of optical properties of solids*, Academic Press Inc., (1985).
- [18] Tompkins, H. G. and Irene, E. A., *Handbook of Ellipsometry*, William Andrew Inc., Springer-Verlag, section 3.4 (2005).
- [19] Press, W. H., Teukolsky, S. A., Vetterling, W. T. and Flannery, B. P., *Numerical Recipes 3rd Edition: The Art of Scientific Computing*, Cambridge University Press, (2007).
- [20] TFCompanion, www.semiconsoft.com.
- [21] Herzinger, C. M., Johs, B., McGahan, W. A. and Woollam, J. A., "Ellipsometric determination of optical constants for silicon and thermally grown silicon dioxide via a multi-sample, multi-wavelength, multi-angle investigation," *J. Appl. Ph.* **83**(6), 3323-3336 (1998).